

# Impact of spatially correlated pore-scale heterogeneity on drying porous media

Oshri Borgman,<sup>1</sup> Paolo Fantinel,<sup>2</sup> Wieland Lühder,<sup>2</sup> Lucas Goehring<sup>2,3</sup>, and Ran Holtzman<sup>1</sup>

<sup>1</sup>Department of Soil and Water Sciences, The Hebrew University of Jerusalem, Rehovot 7610001, Israel

<sup>2</sup>Max Planck Institute for Dynamics and Self-Organization (MPIDS), 37077 Göttingen, Germany

<sup>3</sup>School of Science and Technology, Nottingham Trent University, Clifton Lane, Nottingham, NG11 8NS, UK

## Abstract

We study the effect of spatially-correlated heterogeneity on isothermal drying of porous media. We combine a minimal pore-scale model with microfluidic experiments with the same pore geometry. Our simulated drying behavior compare favorably with experiments, considering the large sensitivity of the emergent behavior to the uncertainty associated with even small manufacturing errors. We show that increasing the correlation length in particle sizes promotes preferential drying of clusters of large pores, prolonging liquid connectivity and surface wetness and thus higher drying rates for longer periods. Our findings improve our quantitative understanding of how pore-scale heterogeneity impacts drying, which plays a crucial role in a wide range of processes ranging from fuel cells to curing of paints and cements to global budgets of energy, water and solutes in soils.

## 1 Introduction

Drying of porous media plays a crucial role in many natural and industrial systems, from soils, to curing of cement, paints and food [Prat, 2011; Goehring *et al.*, 2015]. Drying in soils is of particular environmental importance, as it controls the transfer of water and energy between the subsurface and the atmosphere and affects solute distribution in the root zone [Or *et al.*, 2013]. The rate and extent of fluid transport in general, and drying in particular, intimately depend on the heterogenous distribution of grain and pore sizes and their connectivity, among other factors [Bultreys *et al.*, 2016; Holtzman, 2016]. Pore-size heterogeneity, either random (disordered) or spatially-correlated in the form of patches or layers of finer or coarser particles, is an inherent property of natural porous media such as soils or sediments [Knackstedt *et al.*, 2001], resulting from deposition and diagenetic processes. Even in engineered systems such as micromodels, heterogeneity is inevitable due to manufacturing errors.

In this paper, we investigate how spatial correlation in particle sizes affects isothermal drying of porous media, where evaporation is driven by vapor concentration differences between the medium and the outside atmosphere. Evaporation reduces the liquid pressure, allowing air to invade into the pores once the capillary entry thresholds are exceeded, forming an interface separating liquid- and air-filled pores [Lehmann *et al.*, 2008; Shokri *et al.*, 2010]. The drying process is typically divided into two main stages. During stage 1 (also called “constant rate period”), evaporation occurs mostly from wet patches at the medium’s surface, while liquid is supplied by continuous pathways from the medium’s interior. Stage 1 is characterized by a drying rate which remains fairly constant despite the decline in surface wetness; this is attributed to vapor transport in an air boundary layer that develops outside the medium [Lehmann *et al.*, 2008; Shokri *et al.*, 2010; Shakraeni *et al.*, 2012]. Stage 2 (or the “falling-rate period”) is marked by a disruption of the liquid pathways to the surface, forcing the surface pores to dry out and the evaporation to occur further away from the surface. Consequently, the rate, which becomes limited by vapor diffusion within the porous medium, drops continuously [Lehmann *et al.*, 2008; Shokri *et al.*, 2010; Goehring *et al.*, 2015].

Previous studies have shown that when a sharp contrast in pore sizes exists (in the form of a coarser and a finer region), the coarser region dries up completely before finer pores starts to dry. This has been demonstrated experimentally for a variety of media of different length scales, including sands [Lehmann and Or, 2009; Nachshon et al., 2011; Assouline et al., 2014], micromodels [Pillai et al., 2009] and colloidal drops [Xu et al., 2008]. Theoretically it has been shown that increasing the width of the pore-size distribution prolongs stage 1 by maintaining liquid connectivity for longer periods [Metzger and Tsotsas, 2005; Lehmann et al., 2008]. We note that this observation is true only when gravitational and viscous forces are sufficiently large, e.g. sufficiently long sample. Nonetheless, a systematic study of how the correlation length in sizes (defined as the characteristic length scale over which particles of similar sizes are expected) affects drying is lacking.

For the more general problem of immiscible fluid-fluid displacement, it has been shown that increasing correlation length decreases the residual saturation of the wetting phase at breakthrough [Ioannidis et al., 1993; Knackstedt et al., 2001], leads to a more gradually-varying capillary pressure-saturation relation (retention) [Rajaram et al., 1997; Mani and Mohanty, 1999], and improves connectivity and hence relative permeability of both phases [Mani and Mohanty, 1999]. Changes in retention were also observed upon varying the correlation length of particle wettability in a bead pack [Murison et al., 2014].

Here, we present a systematic investigation of the impact of spatial correlations in particle size on the drying rate and patterns in porous media. We use pore network modeling complemented with microfluidic experiments to obtain a rigorous quantitative analysis and understand the underlying mechanisms. We show that increasing the correlation length promotes preferential invasion, hence preserving liquid connectivity and surface wetness, delaying the transition between the drying stages.

## 2 Methods

One of the main challenges in studying fluid displacement processes such as drying is their large sensitivity to pore-scale details [Bultreys et al., 2016]. This sensitivity typically requires multiple realizations for each set of conditions in order to obtain a statistically-representative description [Mani and Mohanty, 1999]. Here, we formulate a “minimal” model which describes the essential pore-scale physics of this process—including evaporation from interfaces, vapor diffusion, and capillary invasion—via a set of simple rules for interactions between pores. We use this model in computer simulations to generate a sufficiently-large data set to overcome this sensitivity. We further validate our model using microfluidics with unprecedented manufacturing and measurement resolution.

As we seek fundamental understanding of the underlying mechanisms of drying in heterogeneous porous media rather than an accurate quantitative description of specific materials, we choose a simplified analog of a disordered porous medium as our model system. In particular, we use an array of cylindrical solid pillars (“particles”) placed on a regular square lattice, where heterogeneity is achieved by varying the pillar radii. We note that both our experimental and numerical methodologies allow use of other designs, such as a triangular lattice or a random close packing. We consider a horizontal sample to avoid gravitational effects. The sample is open to the atmosphere at one of its faces, from which vapor diffuses outside and air invades into the medium (Fig. 1). Our model is described below, together with a brief description of our microfluidic experiments. For further details of our experiments and a discussion of the ability of such a minimal model to capture the experimental behavior, see [Fantinel et al., 2016].

### 2.1 Pore Network Model

We develop a pore-network model of a drying porous medium, discretizing the pore space into pores (the space between four neighboring pillars) interconnected by throats (the

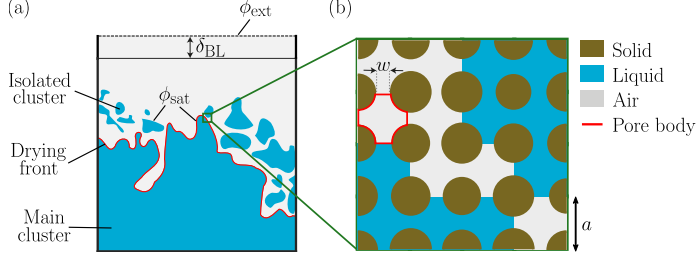


**Figure 1.** Schematics of our model of isothermal drying of a porous sample open to the atmosphere at one of its faces. (a) Low vapor concentration ( $\phi = \phi_{\text{ext}}$ ) at the edge of a diffusive boundary layer (of thickness  $\delta_{\text{BL}}$ ) that develops outside the medium drives evaporation and vapor diffusion away from air-liquid interfaces (where  $\phi = \phi_{\text{sat}}$ ). Evaporation reduces liquid pressure, causing air to invade into liquid-filled pores. Some of the liquid disconnects from the bulk (or the “main cluster”) and becomes isolated. The drying front, namely the leading part of the air-liquid interface (excluding isolated clusters), is marked in red. (b) We model evaporation, vapor diffusion and capillary invasion via a pore network model. Pores (region delimited by red line) are defined as the space between solid particles placed on a square lattice (spacing  $a$ ), and are interconnected by throats (aperture  $w$ ).

constrictions between two adjacent pillars; Fig. 1). Our model also includes an air boundary layer that develops above the medium’s open surface, setting the potential drying rate [Shahraeni *et al.*, 2012]. Evaporation rate is computed from the rate of vapor diffusion away from air-liquid interfaces. This assumption allows us to treat the interface as a source term for vapor, and compute vapor concentrations in the entire domain—air-filled pores as well as the boundary layer—by resolving the mass balance of vapor. A further simplification is provided by the much longer timescale of vapor diffusion relative to that of liquid transport and interface advancement, allowing us to represent the evolution of the drying front as a sequence of steady-state configurations. With this, vapor concentrations are obtained by enforcing the continuity equation in each pore (or boundary layer cell)  $i$ ,

$$\sum_j J_{ij} A_{ij} = 0 \quad (1)$$

where the summation is done over all neighboring pores (or cells)  $j$ , and

$$J_{ij} = -\rho_v^{\text{sat}} D_{\text{eff}} \nabla \phi|_{ij} \quad (2)$$

is the vapor mass flux between two adjacent pores  $i$  and  $j$ , driven by the local gradient of vapor concentration (in terms of relative humidity,  $\phi \in [0, 1]$ ),  $\nabla \phi|_{ij} = (\phi_j - \phi_i)/l_{ij}$ . Throat  $ij$ , connecting pores  $i$  and  $j$ , has a cross-sectional area of  $A_{ij} = hw_{ij}$ , where  $w_{ij}$  is its aperture ( $w_{ij} = a$  for boundary layer cells) and  $h$  is the pillar height (the out of plane sample thickness). Here,  $\rho_v^{\text{sat}}$  is the saturated vapor density.

The distance  $l_{ij}$  is taken to be the lattice spacing  $a$  if both pores are air-filled, and in boundary layer cells. For an air-filled pore  $i$  along the air-liquid interface, we set  $\phi_j = \phi_{\text{sat}} = 1$  as a boundary condition for the diffusion problem, where  $J_{ij}$  represents the local evaporation rate, with  $l_{ij} = a/2$ . Other boundary conditions are fixed concentration,  $\phi = \phi_{\text{ext}} = 0$ , at the external edge of the diffusive boundary layer, and no-flux ( $J = 0$ ) conditions at all faces not open to the atmosphere. This provides a set of coupled linear equations in terms of  $\phi$  in each pore. The effective porous medium diffusion coefficient is  $D_{\text{eff}} = \alpha D$ , where  $D$  is the binary diffusion coefficient of vapor in air, with  $\alpha = 1.6$  inside the porous medium (determined by finite-element simulations at the sub-pore scale) and  $\alpha = 1$  for the boundary layer.

Invasion of air into liquid-filled pores depends on the local capillary pressure, or equivalently, the meniscus curvature (where the two are related via the Young-Laplace law). We

relate the change in curvature to changes in liquid volume by approximating each throat as a cylindrical capillary tube with an effective radius of  $r_{ij}^* = (1/h + 1/w_{ij})^{-1}$ , with a spherical meniscus of curvature  $C$ , such that invasion would occur once the critical curvature for throat  $ij$ ,  $C_{ij}^* = 2/r_{ij}^*$ , has been exceeded,  $C \geq C_{ij}^*$ . Consequently, the curvature of a meniscus  $C$  is linked to the liquid volume evaporated from it,  $\Delta V_{ij}$ , by

$$\Delta V_{ij} = \frac{\pi(2/C)^3}{3} \left(1 - \sqrt{1 - (C/C_{ij}^*)^2}\right)^2 \left(2 + \sqrt{1 - (C/C_{ij}^*)^2}\right). \quad (3)$$

where  $\Delta V_{ij}$  is the cumulative volume decrement relative to a flat meniscus (since  $C = 0$ ). The incremental change in meniscus volume  $ij$  during a single time step  $\Delta t$  is  $\Delta t J_{ij} A_{ij} / \rho_l$ , where  $\rho_l$  is the liquid density. For further details of the derivation of Eq. (3) see Supporting Information.

To resolve the curvatures of all menisci from the evaporated volume, we use the following closure relations: (1) the total liquid volume decrement from the entire cluster equals the sum of volumes decreased from all menisci  $ij$  in that cluster,  $\Delta V_{tot} = \sum_{ij} \Delta V_{ij}$ ; and (2) this deficit is divided between the cluster's menisci such that their curvature  $C$  remains uniform (for all throats). The latter is justified by the much faster pressure diffusion in liquid than of vapor diffusion in air, allowing us to consider instantaneous liquid pressure equilibration. Once a pore is invaded, the liquid volume associated with it is redistributed to other interfacial pores in that cluster, decreasing the cluster's curvature  $C$  according to Eq. (3). Since  $C$  is uniform, every meniscus receives a different volume (according to the corresponding throat radius,  $r_{ij}^*$ ). We restrict the volume of liquid that can be redistributed by enforcing  $C \geq 0$ ; we consider a pore completely dry and advance the interface only once all of its liquid is either redistributed, or, if limited by  $C \geq 0$ , evaporated.

Simulations begin with a liquid-saturated sample. Our computational algorithm is as follows: (i) the evaporation rates from the air-liquid interfaces, for a given interface configuration (invasion pattern), are computed from Eq. (1); (ii) the timestep is the time required to reach the minimal evaporated volume ( $\Delta V_{tot}$ ) corresponding to a meniscus curvature sufficient to invade a throat, determined via Eq. (3); (iii) The interface configuration is updated once the invaded pore empties completely (instantaneously, unless redistribution is restricted). The process is then repeated by returning to step (i), until we reach breakthrough or a desired saturation.

## 2.2 Generating Correlated Geometries

To generate samples with a prescribed spatial correlation in particle sizes,  $\zeta$ , we first create surfaces with correlated topography (where height represents pillar size), by summing 1000 sine waves with random phases and orientations (uniformly distributed), with wave numbers selected from a Gaussian probability distribution. The width of this distribution, in Fourier space, is inversely proportional to  $\zeta$ . We then transform the normally-distributed values into a uniform distribution and rescale to obtain the desired range of pillar sizes,  $R \in [1 - \lambda, 1 + \lambda]\bar{R}$ , where  $\bar{R}$  is the mean pillar radius (overbar denotes arithmetic average) and  $\lambda$  is the imposed disorder.

The following parameter values were used in both simulations and experiments:  $\bar{R} = 50 \mu\text{m}$ ,  $a = 130 \mu\text{m}$ ,  $\bar{w} = 30 \mu\text{m}$  (125 and 25  $\mu\text{m}$  in experiments with  $\zeta = 0$ ),  $h = 40 \mu\text{m}$ , with a mean porosity of 0.53, and sample size of  $100 \times 100$  pillars. The statistical analysis including ensemble averages and standard error in this paper was obtained by generating a set of 40 realizations (namely with a different random seeds) for each  $\zeta$ . In these simulations we used  $\zeta$  values of 0, 1, 1.5, 2, 2.5, 3, 4, 6, 10, and 15,  $\lambda = 0.1$ , and  $\delta_{BL} = 2 \text{ mm}$ . Due to the formation of sample-spanning patches for  $\zeta = 15$ , potentially introducing sample-scale effects, we do not include these simulations in the quantitative analysis along with other  $\zeta$  values. For completeness, experimental and simulated patterns for  $\zeta = 15$  are provided as Supporting Information.

## 2.3 Microfluidic Experiments

Micromodels made of an array of cylindrical pillars in between two planar plates are manufactured using standard microfluidic techniques including soft lithography (for further details see *Fantinel et al.* [2016]). A silicon wafer is spin-coated with a negative photoresist (SU8 3025, MicroChem Corp.), which is then exposed to UV light through a mask to produce the desired design (pillar positions and sizes). After rinsing, the remaining SU8 structure is used as a primer for a secondary mold of polydimethylsiloxane (PDMS). The PDMS is then cured and is used as a mold for the final sample, made of Norland Optical Adhesive 81 (NOA, Sigma-Aldrich). The NOA sample is then cured and exposed to white light to stabilize its optical properties.

Our manufacturing procedure resolution is  $\sim 2 \mu\text{m}$ , with an estimated uncertainty in pillar sizes of  $\sim 1.6 \mu\text{m}$  ( $\sim 3.2\%$  of design). An additional uncertainty, in the boundary layer thickness  $\delta_{\text{BL}}$ , is introduced by bending of the substrate, as well as by an additional layer extending outside the manufactured cell. Thus, to compare with experiments we use in simulations an effective value for  $\delta_{\text{BL}}$ , computed by matching the initial experimental rates. A sensitivity analysis showing how uncertainty in  $\delta_{\text{BL}}$  as well as in other parameters including  $D$ ,  $\rho_v^{\text{sat}}$  and  $\bar{w}/\bar{R}$  impacts drying appears in *Fantinel et al.* [2016]. Samples are filled with a volatile fluorinated oil (Novec 7500 Engineered Fluid,  $\rho_v^{\text{sat}} = 0.35 \text{ kg/m}^3$ ), and placed in a temperature-controlled environment to evaporate, while taking time-lapse images. Images are analyzed to produce discrete, pore-by-pore invasion data and to compute drying rates. Experiments are stopped at breakthrough.

## 3 Results

### 3.1 Comparing Model with Experiments

#### 3.1.1 Drying Patterns

Our simulated drying patterns agree well with patterns in microfluidic experiments using identical pore geometries (Fig. 2a; additional patterns are provided as Supporting Information). The match between a pair of patterns is defined here as the number of overlapping invaded pores (common to both patterns) divided by the average number of invaded pores, at breakthrough. We find an average match of 59%, with a standard deviation of 19%, between our simulations and experiments. Other metrics, including the front roughness and the main cluster saturation, are also in agreement; an exception is the Euler number—the invading phase connectivity computed as the number of clusters of air-filled pores minus the number of liquid clusters (“holes”) within them—which does not [*Fantinel et al.*, 2016]. This disparity is due to isolated liquid clusters that form and persist for longer periods in the experiments (see videos in Supporting Information). Accordingly, when considering the leading front (ignoring small isolated clusters, as often done to estimate finger width [*Toussaint et al.*, 2012]), the pattern match improves (average of 64% with standard deviation of 22%).

#### 3.1.2 Drying Rates

Our simulated drying rates are generally in good agreement with experiments, except for low saturations where simulations exhibit fewer isolated clusters near the surface. Disappearance of near-surface isolated clusters forces the drying front to recede deeper into the medium, and the simulated rate to drop (Fig. 2b). Here,  $e$  is the evaporative flux, in terms of volume of liquid evaporated per time and area of open surface. As experimental rates are computed from the difference in the dry area between consecutive time-lapse images [*Fantinel et al.*, 2016], disagreement in patterns would jeopardize the match in rates. To further examine the impact of the drying pattern on rate, we computed the rates (using Eqs. 1–2) corresponding to the pore-by-pore sequence of experimental patterns. These rates match well the experimental

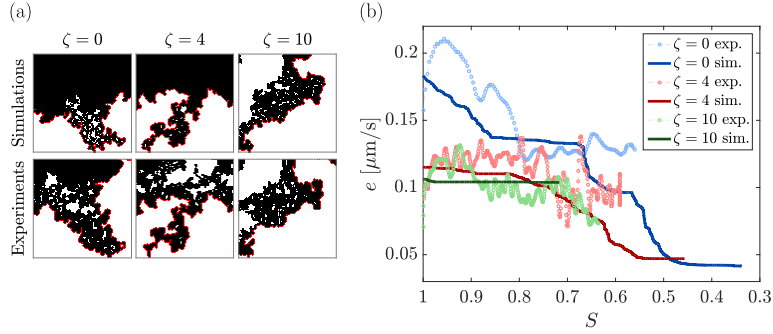


**Figure 2.** (a) Simulated and experimental patterns for samples with different correlation length,  $\zeta$ , are in good agreement. The main difference is the persistence of near-surface isolated clusters for longer periods experimentally. Black and white denote pores filled with air and liquid, respectively (solid not shown); red line indicates the drying front. (b) Simulated drying rates  $e$  initially follow the experimental ones, however with a faster rate drop at lower liquid saturation,  $S$ . This drop is associated with reduced persistence of isolated clusters in simulations, pushing the drying front deeper thus lowering the drying rate.

ones, suggesting that the disparity in patterns is responsible for that in rates; it also confirms the validity of our evaporation and vapor transport calculations.

## 3.2 Impact of Spatial Correlation

### 3.2.1 Drying Patterns

Our simulations demonstrate that increasing the correlation length  $\zeta$  enhances the connectivity of pores of similar size, and hence the accessibility of larger pores across the sample. This promotes preferential drying of larger pores while smaller pores remain wet and maintain liquid connectivity to the surface. As a result, increasing  $\zeta$  forces the drying patterns to follow more closely the underlying pore geometry (Fig. 3a). Here, pore size refers to the volume between four pillars  $I$ ,  $(a^2 - \pi \sum_I R_I/4) h$ . Similarly, the tendency to invade larger pores, quantified here by the fraction of larger-than-average invaded pores (normalized by the total number of invaded pores),  $\chi_L$ , increases with  $\zeta$  (Fig. 3b). Another consequence of preferential drying is that it reaches deeper parts of the medium, leading to an earlier breakthrough, as demonstrated by the increase in the invasion depth  $\bar{Z}_0$  (depth of the center of mass of the invaded pores) with  $\zeta$  (Fig. 3c).

### 3.2.2 Drying Rates

Maintaining liquid connectivity in more correlated samples preserves surface wetness, which, due to its strong influence on drying rates, prolongs stage 1 and delays the rate drop marking the onset of stage 2 [Lehmann et al., 2008; Shokri et al., 2010; Shahraeeni et al., 2012]. Our simulations capture the more gradual decrease in surface wetness, as demonstrated here via a slower drop in surface saturation  $S_{\text{surf}}$  with overall liquid saturation  $S$  in samples with longer correlations  $\zeta$  (Fig. 4a). This results in faster drying, as shown by: (i) maintenance of higher rates  $\tilde{e}$  for longer duration (lower  $S$ , Fig. 4b); and (ii) faster decline of  $S$  with time  $\tilde{t}$  (Fig. 4c). We use the following non-dimensional rate and time:  $\tilde{e} = e/e_0$  where  $e_0 = (\rho_v^{\text{sat}}/\rho_l)D\phi_{\text{sat}}/\delta_{\text{BL}}$  is the potential drying rate, and  $\tilde{t} = t/t_0$  where  $t_0 = nL/e_0$  is the characteristic time to evaporate liquid from a sample of depth  $L$  and porosity  $n$ . The enhancement of drying rate by increasing  $\zeta$  is further quantified through the larger rate at  $S = 50\%$ ,  $\tilde{e}_{50}$ , and shorter time to reach  $S = 50\%$ ,  $\tilde{t}_{50}$  (insets of Fig. 4b–c).

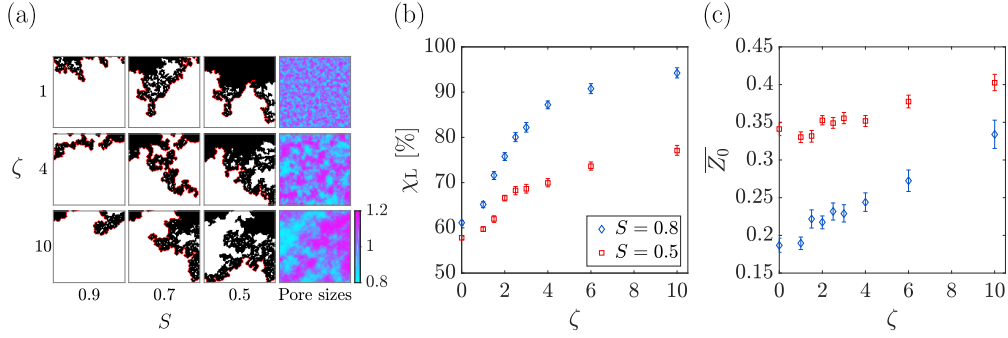


**Figure 3.** (a) Our simulations show that increasing correlation length  $\zeta$  promotes preferential drying of connected large pores, such that the drying pattern follows more closely the underlying sample geometry. Patterns at different liquid saturation,  $S$ , are shown next to the pore size distribution (normalized by the mean). (b) The tendency for preferential drying, quantified here through the fraction of larger-than-average invaded pores,  $\chi_L$  (b), and the mean invasion depth,  $\overline{Z}_0$  (c), increases with  $\zeta$ . Symbols and bars represent ensemble averages and standard error from 40 realizations.

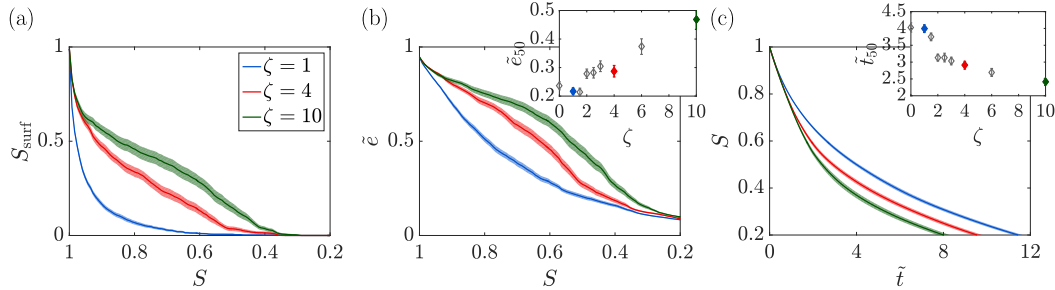


**Figure 4.** Increasing correlation length  $\zeta$  maintains liquid connectivity to the surface, prolonging higher surface wetness,  $S_{\text{surf}}$  (a) and faster drying rates  $\tilde{e}$  for longer duration (b), such that the saturation  $S$  drops faster with time  $\tilde{t}$  (c). Quantitatively, increasing  $\zeta$  increases the rate at  $S = 50\%$ ,  $\tilde{e}_{50}$  (b, inset), and decreases the time to reach  $S = 50\%$ ,  $\tilde{t}_{50}$  (c, inset). For each  $\zeta$  we plot the ensemble average (lines in a–c, diamonds in insets, retaining same colors) and standard error (shading in a–c, error bars in insets) from 40 realizations.

## 4 Discussion

### 4.1 Predictive Model Capabilities: Simulations vs. Experiments

Our simulated patterns are generally in good agreement with microfluidic experiments using similar pore geometry, as quantitatively shown through the agreement in pattern match, front roughness and main cluster saturation. The main difference is the reduced formation and persistence of isolated clusters (quantified via the Euler number) in the simulations, leading to a faster rate drop than observed experimentally. This difference could be attributed in part to wettability effects: a highly-wetting fluid such as the oil used here (contact angle of  $\sim 3^\circ$ ) tends to break into isolated clusters which spread on the solid surfaces (pillars and substrate) [Fantinel *et al.*, 2016]. The presence of liquid films affects vapor diffusion in a complicated manner [Shokri *et al.*, 2010; Prat, 2011; Or *et al.*, 2013] which is outside the scope of this paper. To examine the potential impact of wettability we compare an experiment with oil to one with a less-wetting liquid, water (contact angle of  $\sim 70^\circ$ ). The two experiments mainly differ by the number of isolated clusters, suggesting that wettability effects, which are not included in our model, could potentially decrease the agreement between simulations and experiments [Fantinel *et al.*, 2016].

An inevitable source of disagreement in patterns, and consequently in rates, is manufacturing errors introducing uncertainty in pore geometry. Even with our state-of-the-art manufacturing procedure, small random errors in pillar radius occur ( $\sim 1.6 \mu\text{m}$ ,  $\sim 3.2\%$  of the mean). The emergent patterns—in drying, and, in general, immiscible displacement—are highly sensitive to small geometrical details; that is, slight changes in pore sizes, even locally, can significantly alter the pattern [Bultreys *et al.*, 2016]. An extreme example of this sensitivity is the “binary choice” that can occur when the invasion front reaches a bottleneck in the form of a narrow throat; if slightly altered, the invasion may proceed elsewhere bypassing an entire region. Such a case is presented in the Supporting Information (Fig. S2,  $\lambda = 0.2$ ,  $\zeta = 15$ ), showing distinctively different patterns in samples made from the same mold (identical *design*).

To quantify the sensitivity of the drying pattern to perturbations in pore geometry, we introduce numerically random noise in pillar sizes. Simulations with different noise values (applied to 10 different samples) shows that the pattern match drops to  $\sim 65\%$  when the error reaches 3% (Fig. 5a). The fact that we obtain a comparable match between simulations and experiments indicates that our model predicts patterns very well within the experimental uncertainty in pillar sizes ( $\sim 3.2\%$ , cf. Fig. 5a). To exemplify the impact of uncertainty in geometry, we show how increasing the error introduced to a specific sample design (Fig. 5b) from 1% and 3% reduces the pattern match from 77% to 65%, Figs. 5c and 5d, respectively.

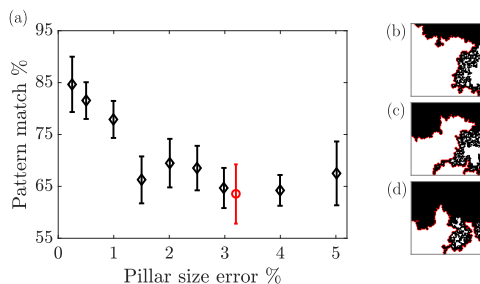


**Figure 5.** Introducing random error in pillar sizes significantly alters the emergent drying patterns, demonstrating their sensitivity to small geometrical details. (a) Our simulations show a reduction in pattern match from  $\sim 85\%$  to  $\sim 65\%$  as the error increases from 0.25% to 1.5% (a, in black, symbols and bars are ensemble averages and standard errors from 10 samples with  $\zeta = 0$ ). Considering the experimental uncertainty in pillar sizes ( $\sim 3.2\%$ ), our simulated patterns agree very well with the experiments (in red, for  $\zeta = 0$ ). The sensitivity to details is exemplified by the alteration of the drying pattern of a particular sample (b) caused by introducing an error of 1% (c) and 3% (d), reducing the match from 77% to 65%, respectively.

## 4.2 Impact of Correlation Length

### 4.2.1 Pressure Evolution

The tendency to preferentially invade large pores, which increases with correlation length, also affects the evolution of the liquid pressure. Each time the invasion front reaches a narrower throat, further decrease in liquid pressure (by evaporation) is required to overcome the large capillary threshold. In a medium with non-correlated heterogeneity, the frequency of such events is high; in contrast, the interconnectivity of pores of similar sizes at high  $\zeta$  reduces the frequency of such events, as exceeding a threshold enables invasion of multiple pores. Indeed, in samples with lower  $\zeta$  we observe a sharper drop in the critical (minimum) pressure  $p_{\text{inv}}$  with saturation  $S$  (Fig. 6); that is, the capillary pressure required for the front to advance becomes larger as drying proceed and  $S$  decreases, in accordance with observations from drainage simulations [Rajaram *et al.*, 1997]. Here  $p_{\text{inv}}$  is the minimum liquid pressure

(Fig. 6, inset), normalized by a characteristic invasion pressure  $p^* = 2\gamma(\bar{w}^{-1} + h^{-1})$ , where  $\gamma$  is the air-liquid interfacial tension.

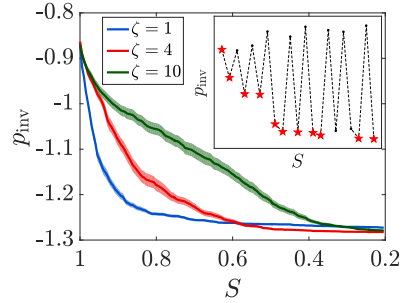


**Figure 6.** In more correlated media (higher  $\zeta$ ), improved connectivity and preferential drying of large pores results in a more gradual change in the invasion pressure,  $p_{\text{inv}}$ . That is, a large number of pores can be invaded without a significant increase in capillary pressure (decrease in liquid pressure). Here  $p_{\text{inv}}$  is the minimum liquid pressure recorded during the drying process, reflecting the critical invasion pressure (inset; minimums marked with red stars). Lines and shading represent ensemble average and standard error from 40 realizations.

#### 4.2.2 Transition Between Drying Stages

Maintaining connectivity of liquid-filled pores impacts the transition between the different drying stages, that is between dominance of evaporation from the open surface, and from deeper parts of the medium's interior [Lehmann *et al.*, 2008]. Our pore-scale model allows us to quantify the relative strength of these mechanisms. We show that increasing spatial correlation delays this transition (Fig. 7), defined here as the saturation at which evaporation rate from the surface equals that from interior pores,  $S_{\text{eq}}$  (Fig. 7, inset). The ability to predict the point of transition between drying mechanisms could be exploited in practice; for instance, one could manipulate the sample's microstructure to control the duration of stage 1 drying [Assouline *et al.*, 2014].

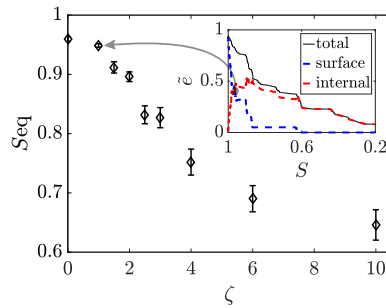


**Figure 7.** The transition between the drying stages is delayed as the correlation length  $\zeta$  increases. The transition is defined here as the saturation at which the evaporation rate from surface pores equals that from internal pores,  $S_{\text{eq}}$ . Diamonds and bars are ensemble average and standard error from 40 realizations. The inset shows the breakup of evaporation rates for a sample with  $\zeta = 1$ ; the crossing of the red and blue lines provides  $S_{\text{eq}}$ .

## 5 Conclusions

We study the impact of spatially-correlated pore geometry on isothermal drying of porous media. We present a minimal pore-scale model, describing evaporation, vapor diffusion, and capillary invasion by a set of simple rules for the interactions between pores. We compare our numerical simulations to state-of-the-art microfluidic experiments using the same pore geometry. Our simulated patterns compare favorably with experiments, especially in light of the large sensitivity of the emergent patterns to uncertainty in pore geometry. We note the reduced formation and persistence of isolated clusters in simulations, leading to a faster drop in the evaporation rate than observed experimentally, which could be explained by wettability effects not included in our model.

We find that increasing the correlation length in particle sizes promotes preferential invasion of large pores, which preserves liquid connectivity and surface wetness, maintaining higher drying rates for longer periods. We explain this behavior by quantifying the point of transition between dominant mechanisms (drying stages): from evaporation mostly at the surface, where rates are controlled by diffusion through the boundary layer, to evaporation from depth at a rate limited by the much slower vapor diffusion inside the porous medium.

Our approach of coupling a minimal pore-scale model with microfluidic experiments as a simple porous media analog, could be applied to study the effects of pore-scale heterogeneity in a wide range of problems including immiscible fluid-fluid displacement [Holtzman, 2016] and solute transport [Kang *et al.*, 2015]. Specifically, our findings improve our understanding of how pore-scale heterogeneity, inevitable in most porous materials, affects their drying rate and extent. These findings bear significant implications for multiple industrial and natural processes, ranging from fuel cells [Prat, 2011], cements and paints [Goehring *et al.*, 2015] to soil-atmosphere energy and moisture exchange and soil salinization [Nachshon *et al.*, 2011; Norouzi Rad *et al.*, 2013; Or *et al.*, 2013].

## Acknowledgments

Financial support by the State of Lower-Saxony, Germany (#ZN-2823) is gratefully acknowledged. RH also acknowledges partial support from the Israeli Science Foundation (#ISF-867/13) and the Israel Ministry of Agriculture and Rural Development (#821-0137-13).

Supporting Information includes details of the derivation of Eq. (3), drying patterns from all microfluidic experiments with corresponding simulated patterns, and videos highlighting the dynamic evolution of the drying pattern in experiments and simulations.

## References

- Assouline, S., K. Narkis, R. Gherabli, P. Lefort, and M. Prat (2014), Analysis of the impact of surface layer properties on evaporation from porous systems using column experiments and modified definition of characteristic length, *Water Resour. Res.*, *50*(5), 3933–3955, doi: 10.1002/2013WR014489.
- Bultreys, T., W. De Boever, and V. Cnudde (2016), Imaging and image-based fluid transport modeling at the pore scale in geological materials: A practical introduction to the current state-of-the-art, *Earth-Sci. Rev.*, *155*, 93–128, doi:10.1016/j.earscirev.2016.02.001.
- Fantinel, P., O. Borgman, R. Holtzman, and L. Goehring (2016), Validating pore-scale models through microfluidic experiments, *arXiv:1612.01897 [physics.flu-dyn]*.
- Goehring, L., A. Nakahara, T. Dutta, S. Kitsunozaki, and S. Tarafdar (2015), *Desiccation cracks and their patterns*, 368 pp., Wiley-VCH, Weinheim, Germany, doi:10.1002/9783527671922.
- Holtzman, R. (2016), Effects of pore-scale disorder on fluid displacement in partially-wettable porous media, *Sci. Rep.*, *6*, 36221, doi:10.1038/srep36221.

- Ioannidis, M. A., I. Chatzis, and E. A. Sudicky (1993), The effect of spatial correlations on the accessibility characteristics of three-dimensional cubic networks as related to drainage displacements in porous media, *Water Resour. Res.*, 29(6), 1777–1785, doi:10.1029/93WR00385.
- Kang, P. K., M. Dentz, T. Le Borgne, and R. Juanes (2015), Anomalous transport on regular fracture networks: Impact of conductivity heterogeneity and mixing at fracture intersections, *Phys. Rev. E*, 92(2), 022148, doi:10.1103/PhysRevE.92.022148.
- Knackstedt, M. A., A. P. Sheppard, and M. Sahimi (2001), Pore network modelling of two-phase flow in porous rock: The effect of correlated heterogeneity, *Adv. Water Resour.*, 24(3-4), 257–277, doi:10.1016/S0309-1708(00)00057-9.
- Lehmann, P., and D. Or (2009), Evaporation and capillary coupling across vertical textural contrasts in porous media, *Phys. Rev. E*, 80(4), 046318, doi:10.1103/PhysRevE.80.046318.
- Lehmann, P., S. Assouline, and D. Or (2008), Characteristic lengths affecting evaporative drying of porous media, *Phys. Rev. E*, 77(5), 056309, doi:10.1103/PhysRevE.77.056309.
- Mani, V., and K. K. Mohanty (1999), Effect of pore-space spatial correlations on two-phase flow in porous media, *J. Petrol. Sci. Eng.*, 23(3-4), 173–188, doi:10.1016/S0920-4105(99)00015-7.
- Metzger, T., and E. Tsotsas (2005), An influence of pore size distribution on drying kinetics : a simple capillary model, *Dry. Technol.*, 23(9-11), 1797–1809, doi:10.1080/07373930500209830.
- Murison, J., B. Semin, J.-C. Baret, S. Herminghaus, M. Schröter, and M. Brinkmann (2014), Wetting heterogeneities in porous media control flow dissipation, *Phys. Rev. Applied*, 2(3), 034002, doi:10.1103/PhysRevApplied.2.034002.
- Nachshon, U., N. Weisbrod, M. I. Dragila, and A. Grader (2011), Combined evaporation and salt precipitation in homogeneous and heterogeneous porous media, *Water Resour. Res.*, 47(3), W03513, doi:10.1029/2010WR009677.
- Norouzi Rad, M., N. Shokri, and M. Sahimi (2013), Pore-scale dynamics of salt precipitation in drying porous media, *Phys. Rev. E*, 88(3), 032404, doi:10.1103/PhysRevE.88.032404.
- Or, D., P. Lehmann, E. Shahraeeni, and N. Shokri (2013), Advances in soil evaporation physics—A review, *Vadose Zone J.*, 12(4), doi:10.2136/vzj2012.0163.
- Pillai, K., M. Prat, and M. Marcoux (2009), A study on slow evaporation of liquids in a dual-porosity porous medium using square network model, *Int. J. Heat. Mass. Tran.*, 52(7-8), 1643–1656, doi:10.1016/j.ijheatmasstransfer.2008.10.007.
- Prat, M. (2011), Pore network models of drying, contact angle, and film flows, *Chem. Eng. Technol.*, 34(7), 1029–1038, doi:10.1002/ceat.201100056.
- Rajaram, H., L. a. Ferrand, and M. a. Celia (1997), Prediction of relative permeabilities for unconsolidated soils using pore-scale network models, *Water Resour. Res.*, 33(1), 43–52, doi:10.1029/96WR02841.
- Shahraeeni, E., P. Lehmann, and D. Or (2012), Coupling of evaporative fluxes from drying porous surfaces with air boundary layer: Characteristics of evaporation from discrete pores, *Water Resour. Res.*, 48(9), W09525, doi:10.1029/2012WR011857.
- Shokri, N., P. Lehmann, and D. Or (2010), Liquid-phase continuity and solute concentration dynamics during evaporation from porous media: Pore-scale processes near vaporization surface, *Phys. Rev. E*, 81(4), 046308, doi:10.1103/PhysRevE.81.046308.
- Toussaint, R., K. Måløy, Y. Méheust, G. Løvøll, M. Jankov, G. Schäfer, and J. Schmittbuhl (2012), Two-phase flow: Structure, upscaling, and consequences for macroscopic transport properties, *Vadose Zone J.*, 11(3), doi:10.2136/vzj2011.0123.
- Xu, L., S. Davies, A. B. Schofield, and D. A. Weitz (2008), Dynamics of drying in 3D porous media, *Phys. Rev. Lett.*, 101, 094502, doi:10.1103/PhysRevLett.101.094502.